

Topological insulators in the NaCaBi family with large SOC gaps

Dexi Shao,¹ Zhaopeng Guo,^{1,2} Xianxin Wu,^{3,1} Simin Nie,⁴ Jian Sun,^{2,5,*} Hongming Weng,^{1,6} and Zhijun Wang^{1,6,†}

¹Beijing National Laboratory for Condensed Matter Physics,

and Institute of Physics, Chinese Academy of Sciences, Beijing 100190, China

²National Laboratory of Solid State Microstructures and School of Physics, Nanjing University, Nanjing 210093, China

³Max-Planck-Institut für Festkörperforschung, Heisenbergstrasse 1, D-70569 Stuttgart, Germany

⁴Department of Materials Science and Engineering,
Stanford University, Stanford, California 94305, USA

⁵Collaborative Innovation Center of Advanced Microstructures, Nanjing 210093, China

⁶University of Chinese Academy of Sciences, Beijing 100049, China

(Dated: March 9, 2021)

By means of first-principles calculations and crystal structure searching techniques, we predict that a new NaCaBi family crystallized into the ZrBeSi-type structure (*i.e.*, $P6_3/mmc$) are strong topological insulators (STIs). Taking $P6_3/mmc$ NaCaBi as an example, the calculated band structure indicates that there is a band inversion between two opposite-parity bands at the Γ point. In contrast to the well-known Bi_2Se_3 family, the band inversion in the NaCaBi family has already occurred even without spin-orbit coupling (SOC), giving rise to a nodal ring surrounding Γ in the $k_z = 0$ plane (protected by M_z symmetry). With time reversal symmetry (\mathcal{T}) and inversion symmetry (\mathcal{I}), the spinless nodal-line metallic phase protected by $[\mathcal{TI}]^2 = 1$ is the weak-SOC limit of the spinful topological insulating phase. Upon including SOC, the nodal ring is gapped, driving the system into a STI. Besides inversion symmetry, the nontrivial topology of NaCaBi can also be indicated by $\bar{6}$ symmetry. More surprisingly, the SOC-induced band gap in NaCaBi is about 0.34 eV, which is larger than the energy scale of room temperature. Four other compounds (KBaBi, KSrBi, RbBaBi and RbSrBi) in the family are stable at ambient pressure, both in thermodynamics and lattice dynamics, even though the gaps of them are smaller than that of NaCaBi. Thus, they provide good platforms to study topological states both in theory and experiments.

I. INTRODUCTION

Topological insulators (TIs) have been studied broadly and deeply in both theory and experiments, since the two-dimensional quantum spin Hall effect (2D TI) was proposed in 2005¹. By generalizing the concept of TIs, the three-dimensional (3D) TIs were predicted in the Bi_2Se_3 family², which were verified in the experiments later³⁻⁵. TIs embody a new quantum state characterized by a topological invariant rather than a spontaneously broken symmetry. The nontrivial topology of TIs is well defined by the wave functions of occupied bands, as long as there is a continuous energy gap between the conduction bands and valence bands in the whole Brillouin zone (BZ). Then, the \mathcal{T} -invariant TIs are generalized to topological crystalline insulators (TCIs)⁶⁻¹⁰, in which the lattice symmetries play important roles. Generally, symmetry eigenvalues and irreducible representations (irreps) can indicate topological property. For example, the well-known Fu-Kane parity indices are widely used for centrosymmetric TIs¹¹, and the recently established symmetry indicators and topological quantum chemistry are very efficient to diagnose the nontrivial topology of TIs and TCIs¹²⁻²⁰. Although many candidates for TIs/TCIs have been proposed, the TIs protected by sixfold rotoinversion symmetry [*i.e.*, the sixfold rotoinversion $\bar{6}$ ($\equiv \mathcal{IC}_6$) is a sixfold rotation (C_6) followed by inversion (\mathcal{I})] are rarely reported.

The 3D TIs have attracted tremendous attention because their surface states possess odd spin-momentum

locked Dirac cones, thus, the backscattering channels of the surface states are suppressed, leading to dissipationless electronic transport^{2,3,21,22}. In proximity to an s -wave superconductor (SC), the topological surface states can acquire an effective p -wave superconducting pairing, resulting in a 2D topological SC²³. In addition, the TIs can be tuned into many interesting topological states. For instance, the quantum anomalous Hall (QAH) insulator is found in the Cr-doped Bi_2Te_3 ^{24,25}. Furthermore, the compound MnBi_2Te_4 is predicted to be an antiferromagnetic TI at zero magnetic field and a Weyl semimetal under the out-of-plane magnetic field²⁶. Recently, the QAH effect has been observed in few-layer thin films²⁷. Moreover, the unconventional SC has been proposed and some experimental evidences were revealed in Cu-doped Bi_2Se_3 ^{28,29}. The strong evidences of Majorana zero-energy mode within a vortex in the TI/SC heterostructure – $\text{Bi}_2\text{Te}_3/\text{NbSe}_2$ – have been proposed recently³⁰. Therefore, the TI candidates are of great interest, especially those with relatively large band gaps, which not only benefit the future applications of spintronics and quantum computation from the dissipationless surface states, but also provide good platforms to study the interplay between the topological phase and symmetry-breaking phases. Though many TI candidates and corresponding interesting properties have been proposed^{2,21,22,31,32}, TIs with relatively large band gaps and clear 2D Dirac-cone surface states as the Bi_2Se_3 family are rare.

In this work, using crystal structure searching techniques and first-principles calculations, we predict that

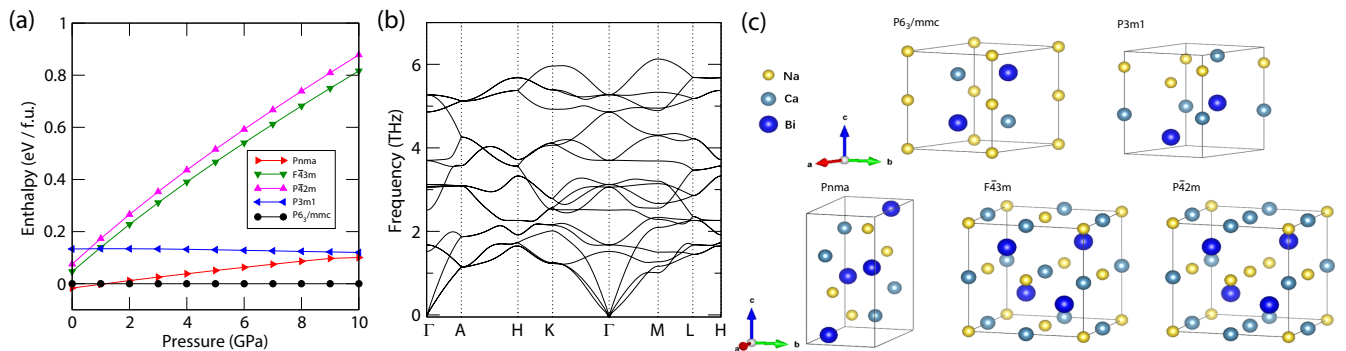


FIG. 1. (a) Calculated enthalpy relative to that of $P6_3/mmc$ phase vs. pressure. (b) Phonon dispersions for the $P6_3/mmc$ phase at the ambient pressure, which justify the lattice dynamical stability of this phase. (c) Five crystal structures crystallized into the $P6_3/mmc$, $P3m1$, $Pnma$, $F\bar{4}3m$ and $P42m$ phases of stoichiometric NaCaBi near the convex hull from the formation enthalpies.

NaCaBi can be stable in the space group (SG) of $P6_3/mmc$ at pressures up to 10 GPa from both the thermal dynamics and the lattice dynamics. Calculations of the band structures indicate that without SOC, $P6_3/mmc$ NaCaBi is a topological semimetal with a nodal ring surrounding the Γ point in the $k_z = 0$ plane. Upon including SOC, the crossing points of the nodal line are all gapped and the system becomes a STI. We find that the nontrivial topology can be indicated not only by inversion symmetry, but also by the $\bar{6}$ symmetry. Moreover, it is exciting that the topologically nontrivial band gap is about 0.34 eV due to strong SOC, which is even larger than the energy scale of room temperature. At last, four other dynamically stable XYBi compounds with similar electronic structures and STI natures are proposed in Section 4 of Appendix.

II. CALCULATIONS AND RESULTS

A. The crystal structures of stoichiometric NaCaBi

We used crystal structure prediction techniques integrated in USPEX³³⁻³⁵ and the machine learning accelerated crystal structure search method³⁶ to find the best candidates of NaCaBi under pressure. From the phase diagrams based on convex hull analysis of formation enthalpies for the Na-Ca-Bi ternary system at 0 GPa and 10 GPa shown in Fig. 5, we find stoichiometric NaCaBi crystallizes in $Pnma$ phase at 0 GPa and $P6_3/mmc$ phase at 10 GPa, respectively. We extract several structures of stoichiometric NaCaBi near the two stable phases from the formation enthalpy, which are in SGs of $P6_3/mmc$, $P3m1$, $Pnma$, $F\bar{4}3m$ and $P42m$, respectively. The enthalpy-pressure ($\Delta H - P$) curves between these phases plotted in Fig. 1(a) exhibit the best ones from our structural predictions at pressures up to 10 GPa. At ambient pressure, the most stable structure of NaCaBi is found to be $Pnma$ phase, and the enthalpy

of $P6_3/mmc$ phase is just 0.17 eV/f.u. higher than that of $Pnma$ phase. Our calculations reveal that $P6_3/mmc$ phase becomes preferred at pressures higher than 1 GPa.

As shown in Fig. 1(b) and Fig. 8, there is no phonon mode with negative frequency in the phonon spectra of $P6_3/mmc$ NaCaBi under pressures from 0 GPa to 10 GPa, which indicates that the metastable $P6_3/mmc$ phase could be quenched to ambient pressure if they can be synthesized at higher pressure. These results are in accordance with the earlier work^{37,38}. As shown in Fig. 7(c), calculations of the ab initio molecular dynamic (AIMD) simulations at ambient pressure and $T = 600$ K indicates that there is no structural collapse after 10 ps (10000 steps). In addition, motivated by earlier works^{39,40}, how the parameters evolves under pressure, strain potential and the possible substrates are also discussed in Section 8 of Appendix. As shown in Fig. 8 and Table VI, we also list many other XYBi compounds in the $P6_3/mmc$ phase which are dynamically stable at low pressures. Besides NaCaBi, other four XYBi compounds (*i.e.*, KBaBi, KSrBi, RbBaBi, and RbSrBi) have similar band structures, thus the same STI nature with NaCaBi (see Section 4 of the Appendix). Different from NaCaBi, the $P6_3/mmc$ phase of KBaBi, KSrBi, RbBaBi and RbSrBi are always energetically preferred from 0 GPa to 10 GPa, as shown in Fig. 6. Moreover, the NaCaBi system possesses the largest inverted band gap, as shown in Table I. In the following, we will focus on NaCaBi with $P6_3/mmc$ phase in the main text.

TABLE I. Band gaps of the NaCaBi family at 0 GPa.

XYBi	NaCaBi	KBaBi	KSrBi	RbBaBi	RbSrBi
Gaps (eV)	0.34	0.22	0.26	0.20	0.25

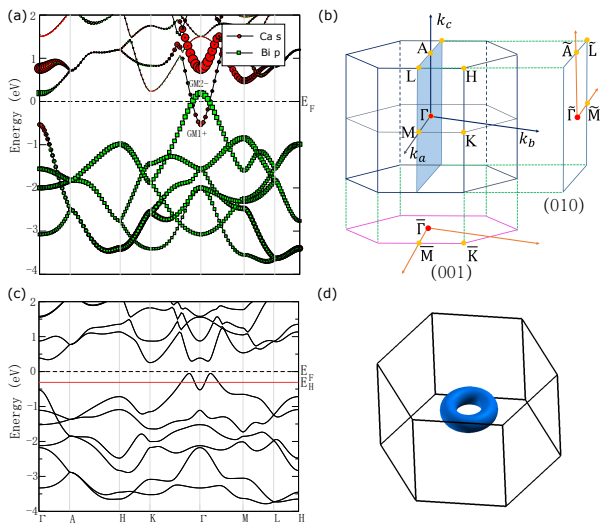


FIG. 2. (a) Orbital-resolved band structures of $P6_3/mmc$ NaCaBi at 0 GPa without SOC. (b) The BZ of $P6_3/mmc$ NaCaBi, where the high-symmetry \vec{k} points are marked out. (c) Band structures of $P6_3/mmc$ NaCaBi at 0 GPa with SOC. The red line corresponds to the 0.06 hole doping case (*i.e.*, $E_H - E_F = -0.25$ eV). (d) The constant-energy contour surface at E_H is a torus.

B. The band structures of $P6_3/mmc$ NaCaBi

From the band structures of $P6_3/mmc$ NaCaBi without SOC shown in Fig. 2(a), we can find two band crossings along $K-\Gamma$ and $\Gamma-M$ at E_F . The orbital-resolved band structures in Fig. 2(a) indicate that the valence band maximum is contributed by the Bi- p states, while the conduction band minimum is from the Ca- s states (which also hybridize with the Bi- s , Na- s and Ca- d states). Calculations of the irreps⁴¹ indicate that the two bands belong to $GM1+$ and $GM2-$ irreps respectively [Fig. 2(a)], in the convention of the Bilbao Crystallographic Server notations at Γ (GM). The parities of the occupied bands at eight time-reversal invariant momenta (TRIMs) are given in Table II. Thus, we conclude that the band inversion appears between opposite-parity bands around Γ without SOC, which guarantees the existence of nodal line(s) in the spinless systems with \mathcal{T} and \mathcal{I} . Furthermore, this nodal ring surrounding Γ lies in the $k_z = 0$ plane due to the presence of M_z symmetry (*i.e.*, the two inverted bands have different M_z eigenvalues).

The spinful topological insulating phase can be considered as a (strong-)SOC limit of the spinless nodal-line metallic phase protected by $[\mathcal{TI}]^2 = 1$ ¹². As shown in Fig. 2(c), we can find that SOC induces a visible band gap between the two inverted bands around Γ , but it does not change the ordering of energy bands at Γ . The nodal ring is fully gapped, thus, the NaCaBi becomes a STI. More surprisingly, the SOC-induced band gap is as large as 0.34 eV, which is comparable with thermal energy of room temperature. The $P6_3/mmc$ phase

TABLE II. The product of the parities for all the occupied bands at the eight TRIMs for the $P6_3/mmc$ phase of NaCaBi.

TRIM	Γ	3M	A	3L	Product
Parity	+	-	-	-	-

of NaCaBi family compounds provides good platforms to study topological states both in theory and experiments. Considering the possible underestimation of the band gap by Perdew-Burke-Ernzerhof (PBE) method⁴², the band inversion can be further confirmed by the calculations using hybrid Heyd-Scuseria-Ernzerhof (HSE) functional⁴³. The results shown in Section 5 of the Appendix indicate that the SOC-induced band gap is almost unchanged, although the inverted gap at Γ (*i.e.*, $E_g \equiv |E_{GM1+} - E_{GM2-}|$) becomes smaller.

Symmetry eigenvalues (or irreps) play key roles in identifying TIs/TCIs in solids¹⁴⁻¹⁶. As we know, SG 194 belongs to a \mathbb{Z}_{12} classification. Using `irvsp`⁴¹ and `Check Topological Mat`²⁰, all symmetry indicators are calculated to be $z_{2w,i=1,2,3} = 0$; $z_4 = 3$; $z_{6m,0} = 5$; $z'_{12} = 11$. By performing the symmetry analysis, we find that there are two essential symmetries indicating the nontrivial topology in this system. One is the inversion symmetry, while the other is the $\bar{6}$ symmetry. In other words, even though the inversion is broken when the SG is reduced to SG 174 ($P\bar{6}$), the nontrivial topology can be still indicated by $z_{3m,0} = 1$ and $z_{3m,\pi} = 0$. With $M_z \equiv [\bar{6}]^3$, these indicate that the mirror Chern numbers of $k_z = 0$ and $k_z = \pi$ planes are 1 and 0, respectively. Thus, this system has to be a 3D STI.

C. The surface states of $P6_3/mmc$ NaCaBi

Exotic topological surface states serve as significant fingerprints to identify various topological phases. Based on the tight-binding model constructed with the maximally localized Wannier functions (MLWFs) and surface Green's function methods⁴⁴⁻⁴⁶, we have calculated the corresponding surface states of this system with SOC to identify its topological properties (see Section 6 of the Appendix). As shown in Figs. 3(a) and 3(b), the 2D Dirac cone is obtained on (010) and (001) surfaces. Thus, the calculated surface states agree well with the analysis of the symmetry indicators, which confirm the STI nature of NaCaBi.

D. Low-energy effective model

We find that the topologically nontrivial nature is determined by the low-energy dispersions near E_F around Γ , which motivates us to build the effective $\mathbf{k} \cdot \mathbf{p}$ Hamiltonian to get further insights in this system. In the presence of SOC, the irreps for the lower energy bands at Γ are Γ_7^\pm

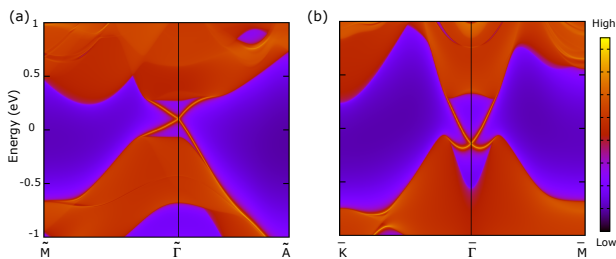


FIG. 3. (a,b) Surface states of NaCaBi terminated in the (010) surface and (001) surface, respectively. Both (010) and (001) surfaces exhibit a 2D Dirac cone.

and Γ_7^- , respectively (labeled in the double point group of D_{6h}).

Thus, we can construct the 4×4 Hamiltonian under the bases of the two irreps (*i.e.*, $|+, \uparrow\rangle; |+, \downarrow\rangle; |-, \uparrow\rangle$ and $|-, \downarrow\rangle$) with the theory of invariants⁴⁷. Here the \pm denote the parities of the eigenstates and \uparrow (\downarrow) denotes $j_z = +\frac{1}{2}$ ($-\frac{1}{2}$). Taking time reversal symmetry and the symmetries of double group D_{6h} into consideration (see details in Section 7 of the Appendix), we derive the following $\mathbf{k} \cdot \mathbf{p}$ invariant Hamiltonian in the vicinity of Γ (up to the second order of \vec{k}),

$$H_0(\vec{k}) = \epsilon_0(\vec{k})\mathbb{I}_4 + \begin{pmatrix} M(\vec{k}) & 0 & A_1 k_z & A_2 k_- \\ 0 & M(\vec{k}) & A_2 k_+ & -A_1 k_z \\ A_1 k_z & A_2 k_- & -M(\vec{k}) & 0 \\ A_2 k_+ & -A_1 k_z & 0 & -M(\vec{k}) \end{pmatrix} \quad (1)$$

where $k_{\pm} = k_x \pm ik_y$, $\epsilon_0(\vec{k}) = C + D_1 k_z^2 + D_2 k_{\perp}^2$ and $M(\vec{k}) = M - B_1 k_z^2 - B_2 k_{\perp}^2$ with $k_{\perp}^2 = k_x^2 + k_y^2$. This is nothing but the well-known 3D TI Hamiltonian in the Bi_2Se_3 family² in the case of $M \cdot B_{1,2} > 0$, the band inversion happens between the two different-parity bands. By fitting the energy dispersions, we obtain the parameters: $M = -0.4554$ eV, $A_1 = 4.0$ eVÅ, $A_2 = 1.3$ eVÅ, $B_1 = -16.7$ eVÅ², $B_2 = 18.6$ eVÅ², $C = -0.0689$ eV, $D_1 = -6.4$ eVÅ², $D_2 = 8.5$ eVÅ².

As aforementioned, the nontrivial topology of this system can be also protected/indicated by $\bar{6}$ symmetry. If we introduce the additional δ_1 (δ_2) term as shown in Eq. (2), C_{2x} (C_{2y}) and M_y (M_x) will be broken. Therefore, by simply adding the two additional terms (both of which break C_{6z} and \mathcal{T}), the $\bar{6}$ -invariant Hamiltonian is obtained below,

$$H(\vec{k}) = H_0(\vec{k}) + H_1(\delta_1 + i\delta_2, \vec{k})$$

$$H_1(z, \vec{k}) = \begin{pmatrix} 0 & 0 & 0 & -z^* k_+^2 \\ 0 & 0 & z k_-^2 & 0 \\ 0 & z^* k_+^2 & 0 & 0 \\ -z k_-^2 & 0 & 0 & 0 \end{pmatrix} \quad (2)$$

In the presence of $\bar{6}$ symmetry, the C_{3z} and M_z symmetries are still preserved. Thus, one can check that in

the case of $M \cdot B_{1,2} > 0$, the mirror Chern number of the $k_z = 0$ plane is 1. On the other hand, one can also compute the symmetry indicators of SG 174 ($P\bar{6}$), which is found to be $z_{3m,0} = 1$. This implies that the \mathbb{Z}_2 invariant for the $k_z = 0$ plane is 1. Combined with the trivial \mathbb{Z}_2 invariant for the $k_z = \pi$ plane, one can conclude that $z_{3m,0} = 1$ and $z_{3m,\pi} = 0$ yield the STI nature of $P6_3/mmc$ NaCaBi. Suppose that we move the two Na atoms at $2a$ Wyckoff positions reversely along z axis a little (*e.g.*, two percent of the third lattice vector along z axis), this distortion preserves $\bar{6}$ symmetry, but breaks inversion symmetry and C_{6z} symmetry. In this disturbed structure, the δ_1 and δ_2 are fitted to be 0.4 eVÅ² and 0 eVÅ². The STI phase is indicated by the symmetry indicators: $z_{3m,0} = 1$ and $z_{3m,\pi} = 0$, since there is no band crossing occurring in this process.

III. DISCUSSION

In carrier-doped TIs, odd-parity pairing and nematic pairing have been theoretically proposed to realize topological superconductivity^{48,49}. Some supporting evidences in Cu-doped Bi_2Se_3 are revealed in experiments but the pairing symmetry is still under active debate^{50–54}. In analogous to Bi_2Se_3 , superconductivity and topological pairing states may be achieved with electron doping in NaCaBi. One prominent feature of $P6_3/mmc$ NaCaBi is that the band inversion is kept with SOC and is significantly large, resulting a double-peak valence band around Γ , as shown in Fig. 2(c). Within a relatively large hole doping region, the Fermi surface is a torus around the Γ point rather than spheres in other TIs, as shown in Fig. 2(d). As the topology of the Fermi surface is distinct from electron-doped case, the pairing state can be also different and may be unconventional. For example, for the intra-orbital spin singlet pairing $c_{+\uparrow}c_{+\downarrow} - c_{-\uparrow}c_{-\downarrow}$, which belongs to a trivial irrep, two nodal lines of gap functions in band space are expected on the torus. We leave the question of determining possible pairing states by solving effective models to future work. Nevertheless, we investigate the superconducting properties by electron-phonon coupling calculations and the Allen-Dynes modified McMillian equation⁵⁵. Considering 0.06 hole doping in NaCaBi system at ambient pressure, T_c is estimated to be about 1.5 K with a commonly used screened Coulomb potential $\mu^* = 0.10$. Most of the contributions to electron-phonon coupling constant arise from the B_{2g} vibrational mode, *i.e.*, vibrations of Ca atoms and Bi atoms along z axis, as shown in Fig. 4(b).

In summary, we propose a new NaCaBi family which are STIs with large SOC-induced band gaps, among which KBaBi, KSrBi, RbBaBi and RbSrBi are stable at ambient pressure, both in thermodynamics and lattice dynamics. In terms of the NaCaBi system, the corresponding symmetry analysis indicates that there exists a clear band inversion between two opposite-parity bands near E_F . Without SOC, the band inversion gives rise to

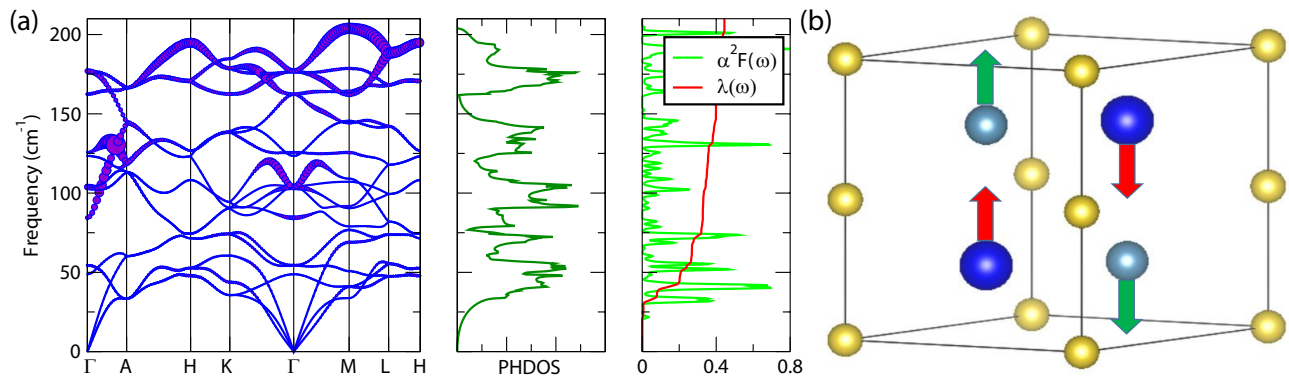


FIG. 4. Electron-phonon coupling calculations of $P6_3/mmc$ NaCaBi. (a) Phonon spectra, phonon density of states (PDOS) and Eliashberg spectral functions $\alpha^2 F(\omega)$ together with the electron-phonon integral $\lambda(\omega)$ in the left, middle and right panels, respectively. (b) The B_{2g} vibrational mode.

a nodal ring around Γ in the $k_z = 0$ plane. Upon including SOC, it becomes a STI with a SOC-induced band gap of 0.34 eV, which is larger than the energy scale of room temperature. The calculated symmetry indicators of SG 194 indicate that the nontrivial topology of NaCaBi can be revealed by not only the inversion symmetry, but also $\bar{6}$ symmetry. As expected, 2D Dirac cones are obtained in the (010)-surface and (001)-surface spectra. Due to the large SOC-induced band gap in the STI phase, it is promising to expect clear experimental evidences of the topological surface states from angle-resolved photoemission spectroscopy (ARPES) and scanning tunnelling microscopy in the future. With hole doping, the contour surface of the valence band near E_F is a torus, which may bring unconventional superconducting pairing.

IV. ACKNOWLEDGMENTS

We thank the fruitful discussions with Lu Liu, Tong Chen and Qinyan Gu. This work is supported by the National Natural Science Foundation of China (Grants Nos. 11974395, 11974162, 11925408, 11834006 and 11921004). J.S. also gratefully acknowledges financial support from the National Key R&D Program of China (Grant Nos. 2016YFA0300404) and the Fundamental Research Funds for the Central Universities. Part of the calculations were carried out using supercomputers at the High Performance Computing Center of Collaborative Innovation Center of Advanced Microstructures, the high-performance supercomputing center of Nanjing University. Z.W. and H.W. also acknowledge support from the National Key Research and Development Program of China (Grant Nos. 2016YFA0300600, 2016YFA0302400, and 2018YFA0305700), the K. C. Wong Education Foundation (GJTD-2018-01), the Strategic Priority Research Program of Chinese Academy of Sciences (Grant No. XDB33000000), and the center for Materials Genome.

APPENDIX

1. Calculation methods

Ab initio calculations. We performed first-principles calculations based on the density functional theory (DFT) using projector augmented wave (PAW) method implemented in the Vienna ab initio simulation package (VASP)⁵⁶ for the calculations of the structure optimization and electronic structures. The generalized gradient approximation (GGA), as implemented in the Perdew-Burke-Ernzerhof (PBE) functional⁴² was adopted. The cutoff parameter for the wave functions was 850 eV. The BZ was sampled by Monkhorst-Pack method⁵⁷ with a k-spacing of $0.025 \times 2\pi \text{ \AA}^{-1}$ for the 3D periodic boundary conditions. The phonon calculations were performed by finite displacement method implemented in the PHONOPY code⁵⁸, with a $2 \times 2 \times 2$ supercell. A kmesh of $20 \times 20 \times 16$ was used to calculate the Fermi surface of the valence band near the Fermi level. Electron-phonon coupling calculations are performed in the framework of Density functional perturbation theory, as implemented in the quantum-espesso code⁵⁹.

2. Crystal structure searching

We perform a variable composition calculation to get the phase diagrams of Na-Ca-Bi ternary system at ambient condition (0 GPa) and 10 GPa. At ambient condition, we find $Pnma$ NaCaBi is the unique ternary phase lying in the convex hull (denoted by the solid red circle in the center of the equilateral triangle), as shown in Fig. 5(a). Meanwhile, there exist three other metastable ternary candidates, i.e., $P4/mmm$ -NaCaBi₂, $Cmmm$ NaCa₂Bi₃ and $R3m$ Na₄CaBi₂, above the convex hull (denoted by the hollow red circles in the the equilateral triangle). The corresponding enthalpies of these metastable ternary candidates above convex hull (denoted by ΔH) of $P4/mmm$

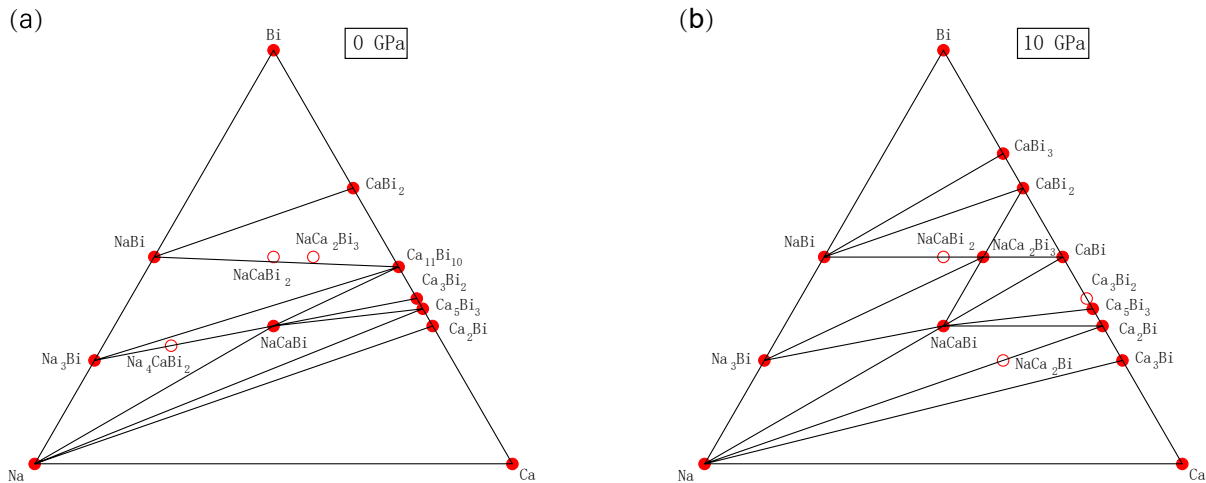


FIG. 5. Phase diagram based on convex hull analysis of formation enthalpies for the Na-Ca-Bi ternary system at (a) 0 GPa and (b) 10 GPa. The solid red circles in the figures denote the stable structures, while the hollow red circles denote the corresponding structures lying above the convex hull which indicates these structures are metastable candidates. The solid red circle in the center of the equilateral triangle in figure (a) and (b) denote the $Pnma$ phase at 0 GPa and $P6_3/mmc$ phase at 10 GPa.

TABLE III. Crystal structures of NaCaBi after structure optimization.

SG	$\{\alpha, \beta, \gamma\}$	$\{a, b, c\}$	Wyckoff positions
$P6_3/mmc$	$\alpha = \beta = 90^\circ, \gamma = 120^\circ$	$\{a = b = 5.566\text{\AA}, c = 6.804\text{\AA}\}$	$\{2a, 2c, 2d\}$
$P3m1$	$\alpha = \beta = 90^\circ, \gamma = 120^\circ$	$\{a = b = 5.3431\text{\AA}, c = 7.41\text{\AA}\}$	$\{1a \oplus 1c, 1b \oplus 1c, 1a \oplus 1b\}$
$Pnma$	$\alpha = \beta = \gamma = 90^\circ$	$\{a = 8.088\text{\AA}, b = 4.784\text{\AA}, c = 9.681\text{\AA}\}$	$\{4c, 4c, 4c\}$
$F\bar{4}3m$	$\alpha = \beta = \gamma = 90^\circ$	$\{a = b = c = 7.530\text{\AA}\}$	$\{4a, 4b, 4c\}$
$P42m$	$\alpha = \beta = \gamma = 90^\circ$	$\{a = b = 7.5706\text{\AA}, c = 7.5032\text{\AA}\}$	$\{1a \oplus 1b \oplus 2f, 1c \oplus 1d \oplus 2e, 4n\}$

1. The “SG” column denotes the space group in which NaCaBi crystallises into.
2. $\{\alpha, \beta, \gamma\}$ and $\{a, b, c\}$ denote the lattice parameters of the conventional cell (while not primitive cell) in each phase.
3. The “Wyckoff positions” column gives the Wyckoff positions of Na, Ca and Bi in each phase. “ $1a \oplus 1c$ ”, “ $1b \oplus 1c$ ” and “ $1a \oplus 1b$ ” in $P3m1$ phase indicates that there exist two nonequivalent “Na”/“Ca”/“Bi” atoms occupying $(1a \text{ and } 1c)/(1b \text{ and } 1c)/(1a \text{ and } 1b)$ Wyckoff positions in this phase, respectively.

NaCaBi_2 , $Cmmm$ NaCa_2Bi_3 and $R3m$ Na_4CaBi_2 are 16.0 meV/atom, 13.3 meV/atom and 19.7 meV/atom, respectively. We have listed the structure parameters of these ternary structures in Table. IV.

At 10 GPa, we find $P6_3/mmc$ NaCaBi and $Cmmm$ NaCa_2Bi_3 (denoted by two solid red circles lying inside the equilateral triangle) are two stable ternary structures lying in the convex hull, as shown in Fig. 5(b). In addition, the convex hull analysis indicates that there are three other structures ($C2/m$ Ca_3Bi_2 , $Cmmm$ NaCaBi_2 and $P4/mmm$ NaCa_2Bi) lying above the convex hull, which indicates they are metastable candidates. The corresponding structure parameters are listed in Table. V. It should be noted that $C2/m$ Ca_3Bi_2 and $Cmmm$ NaCaBi_2 are metastable candidates with only 0.64 meV/atom and 1.2 meV/atom above the convex hull. We also remind that binary Na-Bi and binary Ca-Bi phases in the convex hull are almost in accordance with earlier works^{60,61}.

We do not perform ternary structural searching for the other four XYBi candidates, because it will be time consuming. But, similar with NaCaBi, the thermal stability between the $P6_3/mmc$ phase and the $Pnma$ phase are discussed. As shown in Fig. 6, the $Pnma$ phase of NaSrBi is always preferred under pressures from 0 GPa to 10 GPa, while for cases of KBaBi, KSrBi, RbBaBi and RbSrBi, the $P6_3/mmc$ phase are always preferred. It means the STI phase can be obtained in the KBaBi, KSrBi, RbBaBi and RbSrBi systems without any quenched progress.

3. Molecular dynamics

To check the thermal stability of $P6_3/mmc$ NaCaBi, we have performed ab initio molecular dynamic (AIMD) simulations with a $3 \times 3 \times 2$ supercell at ambient pressure and $T = 600$ K. As shown in Fig. 7(c), no structural

TABLE IV. Crystal structures of Na-Ca-Bi ternary system near the convex hull at ambient condition.

SG	$\{\alpha, \beta, \gamma\}$	$\{a, b, c\}$	Wyckoff positions	ΔH
$Pnma$ -NaCaBi	$\alpha = \beta = \gamma = 90^\circ$	$\{a = 8.088\text{\AA}, b = 4.784\text{\AA}, c = 9.681\text{\AA}\}$	$\{4c, 4c, 4c\}$	0
$P4/mmm$ -NaCaBi ₂	$\alpha = \beta = \gamma = 90^\circ$	$\{a = b = 5.2019\text{\AA}, c = 9.6268\text{\AA}\}$	$\{1c, 1a, 2e\}$	16
$Cmmm$ -NaCa ₂ Bi ₃	$\alpha = \beta = \gamma = 90^\circ$	$\{a = 15.2393\text{\AA}, b = 5.1890\text{\AA}, c = 4.5445\text{\AA}\}$	$\{2a, 4g, 4h \oplus 2c\}$	13.3
$R3m$ -Na ₄ CaBi ₂	$\alpha = \beta = 90^\circ, \gamma = 120^\circ$	$\{a = b = 5.4382\text{\AA}, c = 26.6190\text{\AA}\}$	$\{3a \oplus 3a \oplus 3a \oplus 3a, 3a, 3a \oplus 3a\}$	19.7

1. ΔH column is under the unit of meV.

TABLE V. Crystal structures of Na-Ca-Bi ternary system near the convex hull at 10 GPa.

SG	$\{\alpha, \beta, \gamma\}$	$\{a, b, c\}$	Wyckoff positions	ΔH
$P6_3/mmc$ -NaCaBi	$\alpha = \beta = 90^\circ, \gamma = 120^\circ$	$\{a = b = 5.1857\text{\AA}, c = 6.2652\text{\AA}\}$	$\{2a, 2c, 2d\}$	0
$Cmmm$ -NaCa ₂ Bi ₂	$\alpha = \beta = \gamma = 90^\circ$	$\{a = 14.6714\text{\AA}, b = 4.7828\text{\AA}, c = 4.3440\text{\AA}\}$	$\{2a, 4g, 4h \oplus 2c\}$	0
$Cmmm$ -NaCaBi ₂	$\alpha = \beta = \gamma = 90^\circ$	$\{a = 6.7302\text{\AA}, b = 8.7712\text{\AA}, c = 3.3638\text{\AA}\}$	$\{2c, 2d, 4e\}$	1.2
$P4/mmm$ -NaCa ₂ Bi	$\alpha = \beta = \gamma = 90^\circ$	$\{a = b = 4.7903\text{\AA}, c = 4.3642\text{\AA}\}$	$\{2c, 2d, 4e\}$	9.5

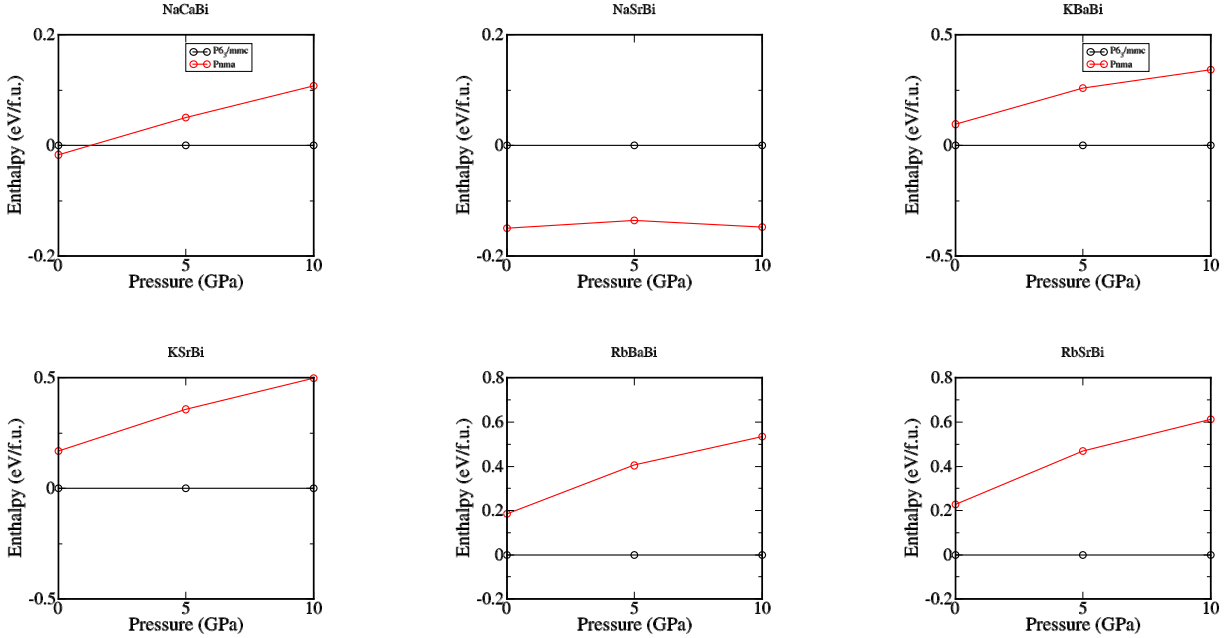


FIG. 6. Calculated enthalpy between the $Pnma$ phase and $P6_3/mmc$ phase vs. pressure for NaCaBi, NaSrBi, KBaBi, KSrBi, RbBaBi and RbSrBi, respectively.

collapse was observed after 10 ps (10000 steps), which indicates the thermal stability of NaCaBi at ambient pressure.

4. Phonon spectra and band structures of XYBi compounds with $P6_3/mmc$ structure under low pressures

According to the online Materials Project⁶³ database, the Inorganic Crystal Structure Database⁶⁴ and the ear-

lier work³⁷, RbHgSb and several XYBi systems with $X = \{\text{Na, K, Rb}\}$ and $Y = \{\text{Mg, Ca, Sr, Ba, Zn, Cd, Hg}\}$ can crystallise into the ZrBeSi-type structure of $P6_3/mmc$. We performed calculations in terms of the lattice dynamical stability for them at 0 GPa, 5 GPa and 10 GPa, respectively. Among, only the dynamically stable ones are listed in Table VI. Their phonon spectra and band structures are giving in Fig 8. From Fig 8, we can find they are mainly classified into three classes: the KHgSb-type TCI phase⁹ (*i.e.*, KZnBi, RbCdBi, RbHgSb, RbZnBi), the Na₃Bi-type Dirac phase⁶⁵ (*i.e.*, NaZnBi, NaCdBi and

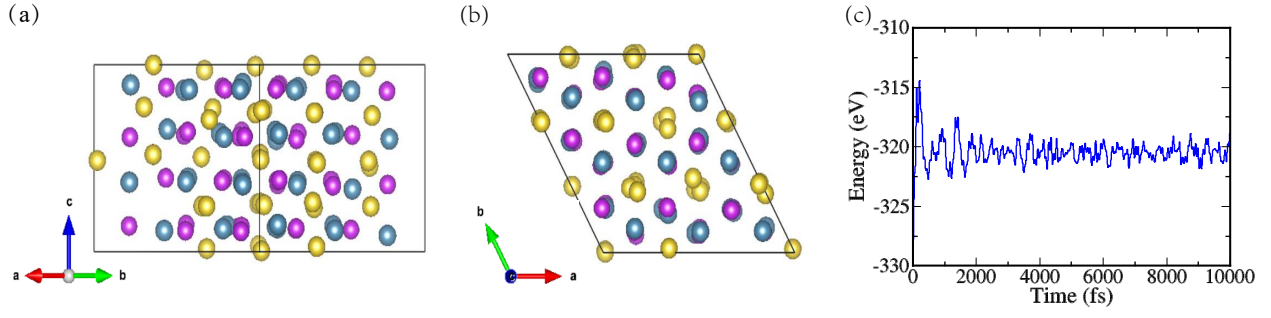
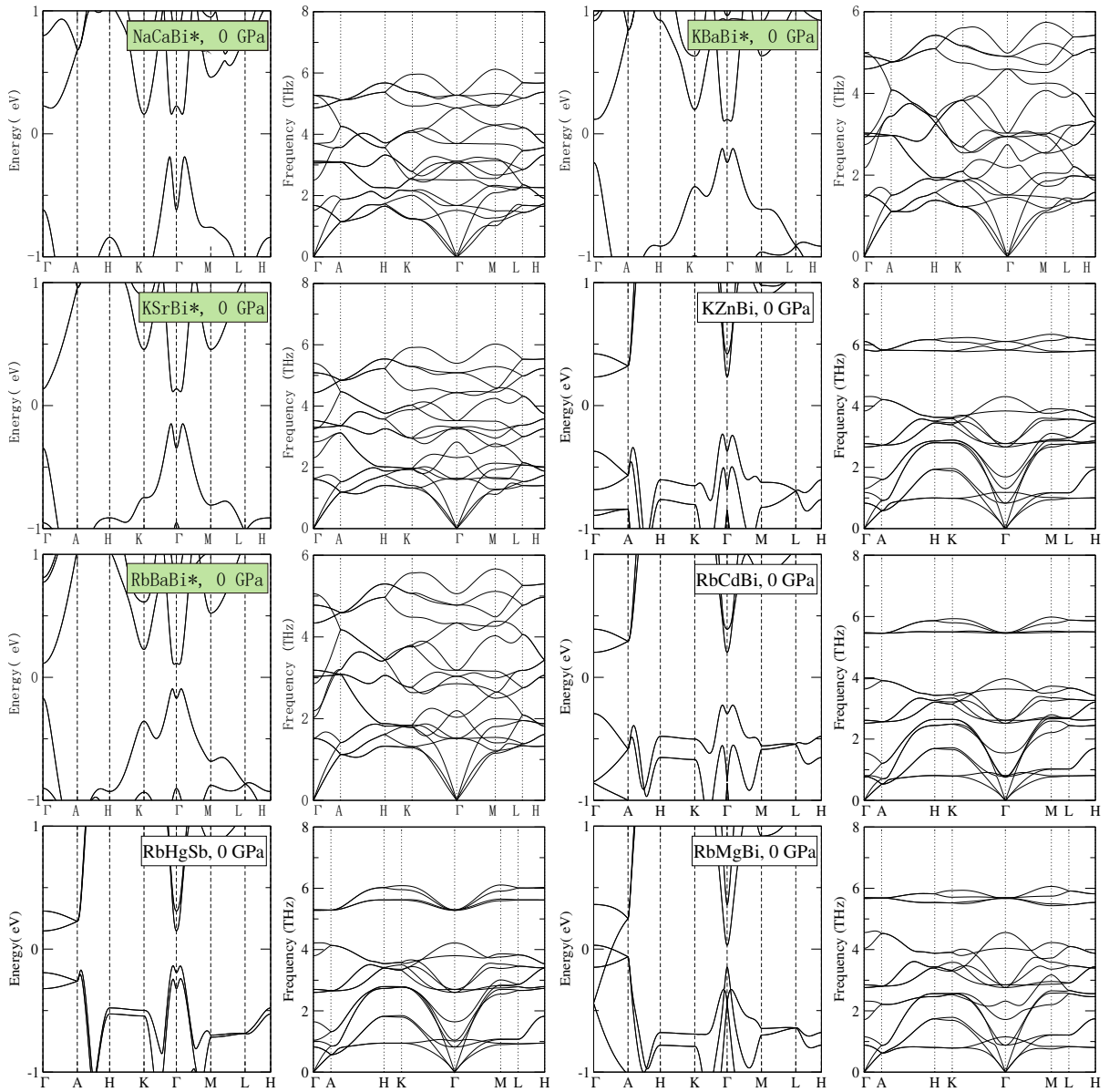
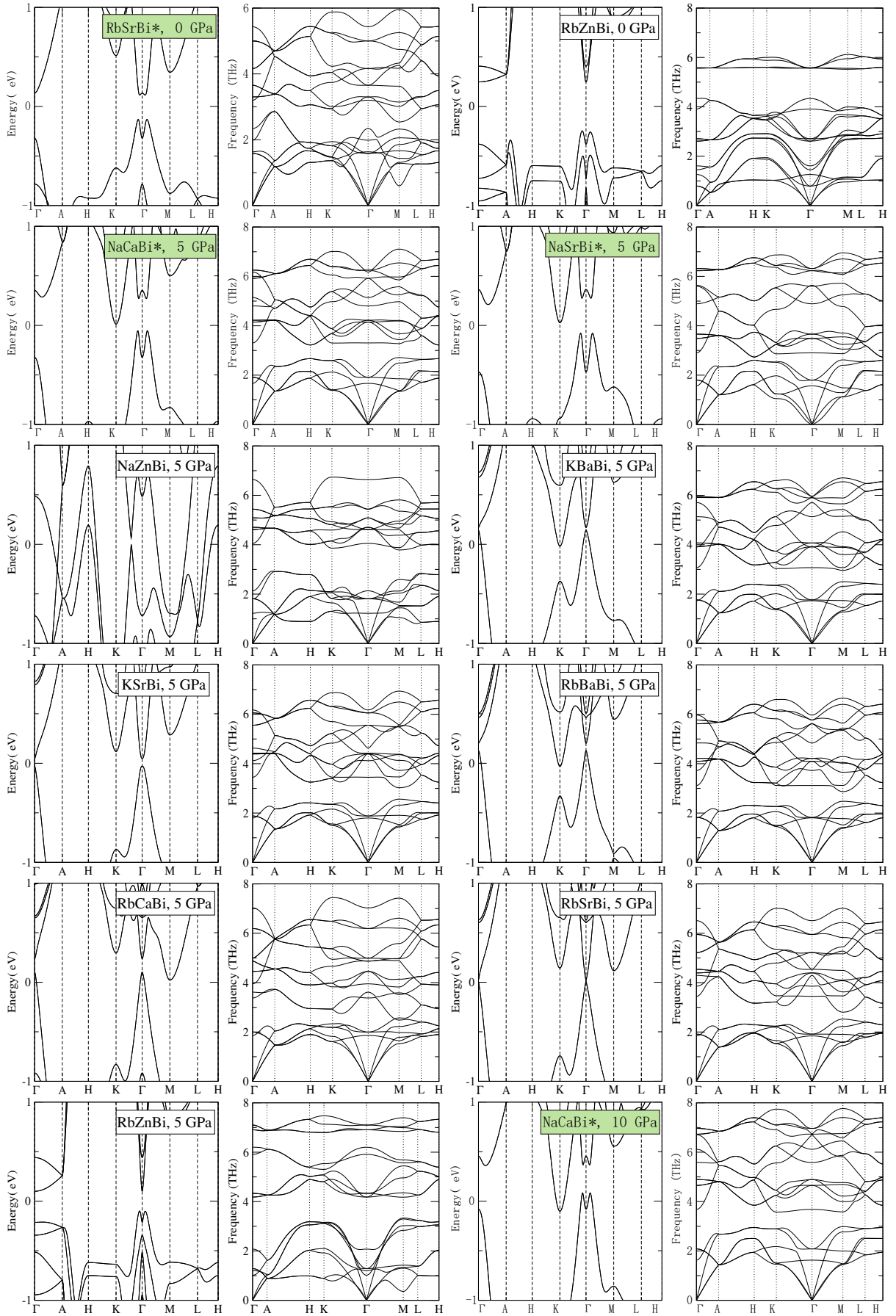


FIG. 7. After 10 ps AIMD simulation, the side view (a) along (001) direction and (b) along (110) direction of the $3 \times 3 \times 2$ supercell of NaCaBi at 600 K. (c) The NVT-molecular dynamic (MD) simulations of the NaCaBi at static pressure and $T = 600$ K.





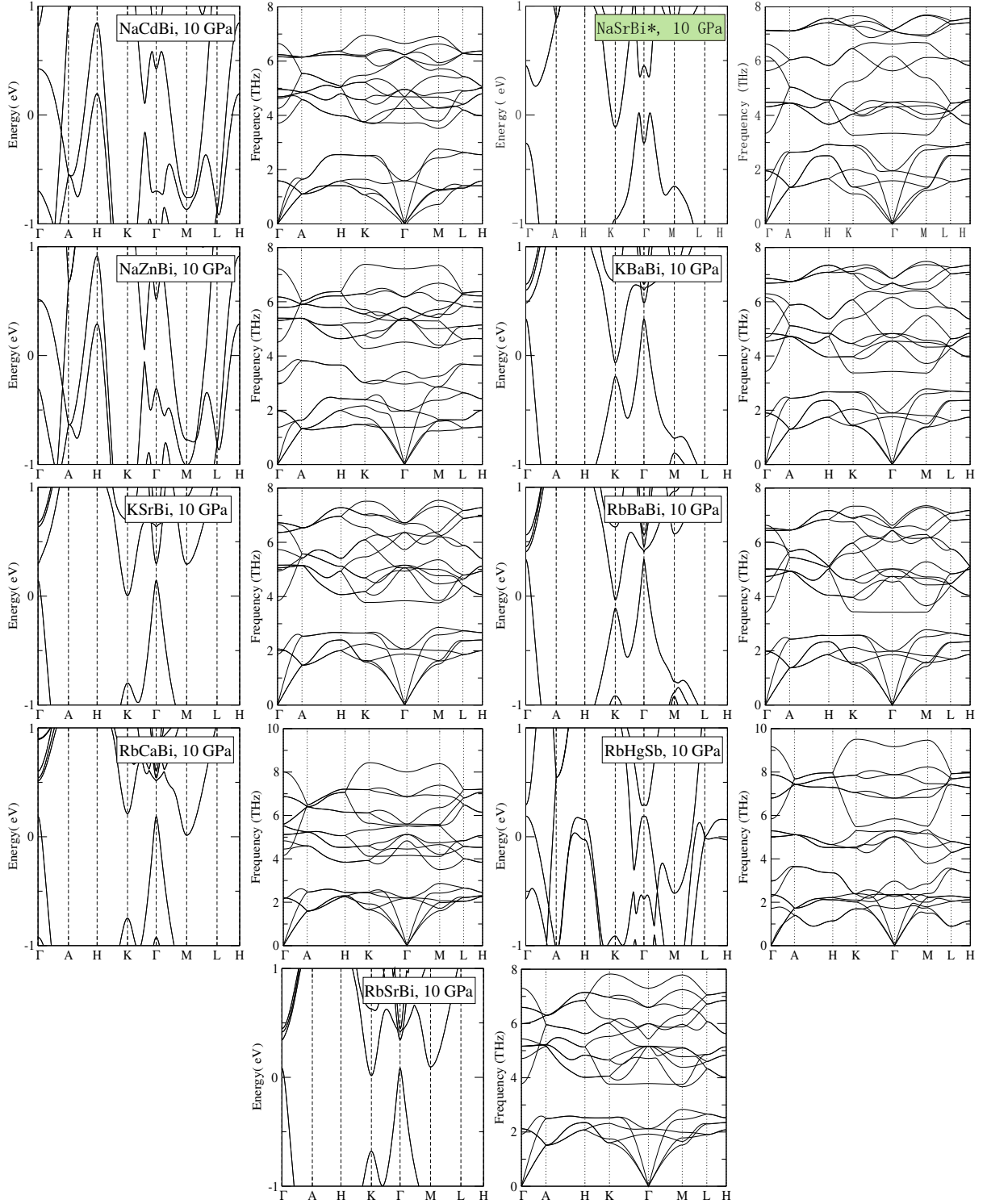


FIG. 8. Band structures and phonon spectra of $P6_3/mmc$ RbHgSb and XYBi when they are dynamically stable under 0 GPa, 5 GPa and 10 GPa, respectively. Our calculations reproduce the Dirac point in the $P6_3/mmc$ RbMgBi system⁶².

TABLE VI. Dynamically stable RbHgSb and XYBi systems at 0 GPa, 5 GPa and 10 GPa, respectively.

Pressure(GPa)	RbHgSb and XYBi systems
0 GPa	NaCaBi*,KBaBi*,KSrBi*,KZnBi,RbBaBi*,RbCdBi,RbHgSb,RbMgBi,RbSrBi*,RbZnBi
5 GPa	NaCaBi*,NaSrBi*,NaZnBi,KBaBi,KSrBi,RbBaBi,RbCaBi,RbSrBi,RbZnBi
10 GPa	NaCaBi*,NaCdBi,NaSrBi*,NaZnBi,KBaBi,KSrBi,RbBaBi,RbCaBi,RbHgSb,RbSrBi

Structures with “*” behind denote those possessing similar band structures with $P6_3/mmc$ NaCaBi.

RbMgBi) and the STI phase. Since we are focused on the STI phase, several of these dynamically stable compounds of the STI phase, having the similar band structures with $P6_3/mmc$ NaCaBi in the main text, are denoted by “*” symbols.

5. HSE calculations

It is known that the PBE functional tends to underestimate the band gap, we recalculated the band structures of $P6_3/mmc$ NaCaBi system with the HSE06 functional⁴³, as shown in Fig. 9. We find the energy dispersions for low energy bands using the HSE06 functional is similar to that using PBE functional, which indicates that the topological nature is solid.

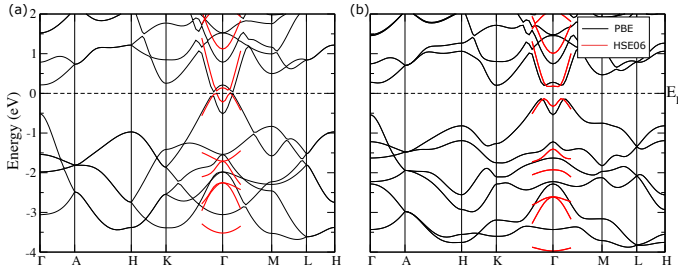


FIG. 9. HSE band structures in comparison with DFT band structures.

6. Wannier-based tight-binding model and surface states

Surface state plays an important role on justifying/characterizing TIs from the bulk-boundary correspondence. Here we choose Ca-*s*, Ca-*d* and Bi-*p* as the projected orbits to build the Wannier-based tight-binding model, it reproduces the DFT band structures well, as shown in Fig. 10. Then, we calculated the surface states based on this Wannier-based tight-binding model of NaCaBi on the (010) and (001) surfaces, as presented in Fig. 3 in the main text.

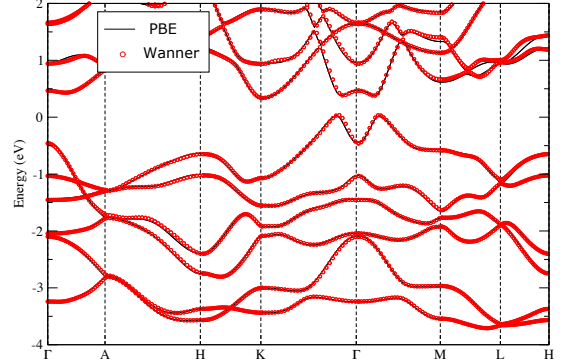


FIG. 10. DFT vs Wannier bands.

7. Matrix presentations of symmetry operators

Under the basis of Γ_7^+ and Γ_7^- , the symmetry operators (*e.g.*, \mathcal{T} , \mathcal{I} , C_{6z} , C_{2x} , C_{2y}) are represented below:

$$\begin{aligned} \mathcal{T} &= \tau_0 \otimes (-i)\sigma_y \mathcal{K}; \quad \mathcal{I} = \tau_z \otimes \sigma_0; \quad C_{6z} = \tau_0 \otimes e^{-i\frac{\pi}{3}\sigma_z}; \\ C_{2x} &= \tau_0 \otimes (-i)\sigma_x; \quad C_{2y} = \tau_0 \otimes (-i)\sigma_y, \end{aligned} \quad (3)$$

where \mathcal{K} denotes the complex conjugation, $\tau_{x,y,z}$ ($\sigma_{x,y,z}$) are Pauli matrices in the orbital (spin) space. Their ($\mathcal{O} = P, Q, R, \mathcal{T}$) representations in momentum space are given by $\mathcal{O}[k_x, k_y, k_z]^T = g_{\mathcal{O}}[k_x, k_y, k_z]^T$

$$\begin{aligned} g_{\mathcal{T}} = g_{\mathcal{I}} &= \begin{pmatrix} -1 & 0 & 0 \\ 0 & -1 & 0 \\ 0 & 0 & 1 \end{pmatrix}, \quad g_{C_{6z}} = \begin{pmatrix} \frac{1}{2} & -\frac{\sqrt{3}}{2} & 0 \\ \frac{\sqrt{3}}{2} & \frac{1}{2} & 0 \\ 0 & 0 & 1 \end{pmatrix}, \\ g_{C_{2x}} &= \begin{pmatrix} 1 & 0 & 0 \\ 0 & -1 & 0 \\ 0 & 0 & -1 \end{pmatrix}, \quad g_{C_{2y}} = \begin{pmatrix} -1 & 0 & 0 \\ 0 & 1 & 0 \\ 0 & 0 & -1 \end{pmatrix}. \end{aligned} \quad (4)$$

The low-energy effective $\mathbf{k} \cdot \mathbf{p}$ Hamiltonian satisfies the condition placed by the symmetry \mathcal{O} :

$$\mathcal{O}\mathcal{H}(\delta\mathbf{k})\mathcal{O}^{-1} = \mathcal{H}(g_{\mathcal{O}}\delta\mathbf{k}) \quad (5)$$

After considering all symmetry restrictions of D_{6h} , the low-energy effective model is derived as given in the main text.

8. Pressure, Strain and substrate candidates

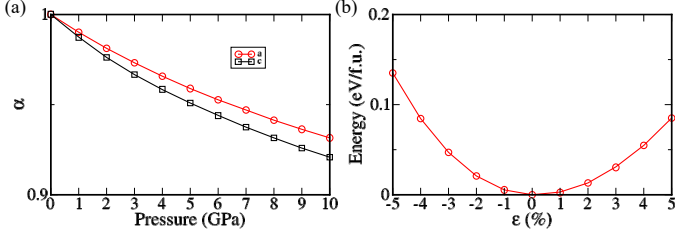


FIG. 11. (a) Lattice parameters $a(= b)$ and c vs. Pressure. (b) Strain energy vs. the linear biaxial strain along the x and y axes.

From the electronic properties of $P6_3/mmc$ NaCaBi at 0 GPa, 5 GPa and 10 GPa shown in Fig. 8, we find that there is an electron pocket of the conduction band around K dropping to the Fermi level quickly under pressure. And when the applied pressure is as large as 10 GPa, this pocket goes across the Fermi level, which leads $P6_3/mmc$ NaCaBi to be a metal. As shown in Fig. 11(a), we can find the lattice parameters $a(= b)$ and c decrease under pressure. Moreover, the lattice parameters a/c decrease about 1%/1.3% at 1 GPa, from which the $P6_3/mmc$ phase of NaCaBi becomes preferred. It should also be noted that though the $P6_3/mmc$ NaCaBi changes from an insulator to a metal from 0 GPa to 10 GPa, the inverted direct gap is always kept. Thus, the STI nature with topological surface states is kept up to 10 GPa.

Looking along the c axis, the $P6_3/mmc$ NaCaBi is a layered hexagonal structure with its layer lying in the xy plane. Thus, we can introduce substrates perpendicular to the layer plane. As shown in Table VII, we have introduced 31 substrates with the lattice mismatch less than 1% along the x and y axes to assist growth teams attempting to synthesize the $P6_3/mmc$ phase of NaCaBi. Some commonly used crystals such as KTiO_3 and BaNiO_3 only have lattice mismatch with NaCaBi of about -0.1% and 0.3%, which are very small and can be good substrate candidates. However, it should be noted that, as theoreticians, our proposal is very rough and more complicated experimental details should be considered before real experiments.

Similar with applying pressure, imposing various strains are also considered as convenient methods to tune the electronic properties in the condensed systems. Here we focus on applying biaxial linear strain along a and b axes which keeps the symmetries of this system unchanged. From Fig. 11(b), we find the strain energy of this kind of biaxial linear strain increase parabolically with $-5\% \leq \epsilon \leq 5\%$, which indicates this kind of strain can be seen as elastic strain in a very large range. Thus, it offers the experimental team large degree of freedom to choose potential substrates candidates.

TABLE VII. 31 substrate candidates with the lattice mismatch less than 1% with the $P6_3/mmc$ phase of NaCaBi.

Formula	No-MP	No-ICSD	Band gap(eV)	a(Å)	Mismatch(ϵ)
KAl(MoO ₄) ₂	mp-19352	28018	3.890	5.545	-0.4%
AlTi(MoO ₄) ₂	mp-18733	250339	3.871	5.544	-0.4%
CsAl(MoO ₄) ₂	mp-505784	280947	3.879	5.551	-0.3%
RbFe(MoO ₄) ₂	mp-563010	245666	2.572	5.596	0.5%
HfPd ₃	mp-11453	638769, 104254	0	5.595	0.5%
KTiO ₃	mp-1180658	94775	0	5.560	-0.1%
KAg ₂	mp-12735	150142	0	5.589	0.4%
Na ₂ LiAu ₃	mp-12815	152090	0	5.530	-0.6%
BaNiO ₃	mp-19138	175, 30661	1.542	5.580	0.3%
Ce ₂ In	mp-19733	621365, 621356, 102186	0	5.557	-0.2%
Sm ₂ In	mp-19816	59527, 59526, 640547, 640544	0	5.549	-0.3%
Pr ₂ In	mp-19854	640268, 108555	0	5.558	-0.1%
Nd ₂ In	mp-21295	59423, 59422, 59421, 640067	0	5.589	0.4%
CaAl ₁₂ O ₁₉	mp-28234	34394	4.320	5.564	\approx 0%
Rb ₂ Te	mp-383	55157, 55152, 55160, 55154...	1.372	5.574	0.1%
In ₂ Pt ₃	mp-510439	640295, 59498, 640287	0	5.575	0.2%
SmOs ₂	mp-570007	150521	0	5.574	0.1%
TaPd ₃	mp-582360	648968	0	5.520	-0.8%
PF ₅	mp-8511	62554	7.109	5.563	\approx 0%
Ba ₃ BPO ₃	mp-9712	402017	1.471	5.502	-1.1%
Ba ₃ BAOs ₃	mp-9793	402682	1.529	5.528	-0.7%
LaAl ₂ Ag ₃	mp-16766	57329	0	5.565	\approx 0%
Na ₃ OsO ₅	mp-555476	416999	0.113	5.553	-0.2%
Li ₂ Ta ₂ (OF ₂) ₃	mp-561011	405777	3.835	5.581	0.3%
Sr ₂ MgH ₆	mp-644225	88205	2.758	5.546	-0.4%
LaBPt ₂	mp-31052	98425	0	5.522	-0.8%
LaB ₂ Ir ₃	mp-10112	44422	0	5.543	-0.4%
BaPd ₅	mp-2606	58672, 616030	0	5.540	-0.5%
NaBPt ₃	mp-28614	68092	0	5.547	-0.3%
CaB ₂ Rh ₃	mp-28705	66767	0	5.551	-0.3%
SrZn ₅	mp-638	106114, 418615	0	5.541	-0.4%

1. No-MP column denotes the materials ID recorded in the Materials Project, while No-ICSD column denotes the materials ID recorded in the ICSD.
2. $\epsilon > 0$ denotes the lattice parameter a of the substrate candidate is larger than that of $P6_3/mmc$ NaCaBi, while $\epsilon < 0$ denotes the lattice parameter a of the substrate candidate is smaller than that of $P6_3/mmc$ NaCaBi.

- * Corresponding author. Email: jiansun@nju.edu.cn
- † Corresponding author. Email: wzj@iphy.ac.cn
- ¹ Kane, C. L. & Mele, E. J. Quantum Spin Hall Effect in Graphene. *Phys. Rev. Lett.* **95**, 226801 (2005).
 - ² Zhang, H. *et al.* Topological insulators in Bi₂Se₃, Bi₂Te₃ and Sb₂Te₃ with a single Dirac cone on the surface. *Nat. Phys.* **5**, 438–442 (2009).
 - ³ Hsieh, D. *et al.* A tunable topological insulator in the spin helical Dirac transport regime. *Nature* **460**, 1101–1105 (2009).
 - ⁴ Xia, Y. *et al.* Observation of a large-gap topological-insulator class with a single Dirac cone on the surface. *Nat. Phys.* **5**, 398 (2009).
 - ⁵ Chen, Y. L. *et al.* Experimental Realization of a Three-Dimensional Topological Insulator, Bi₂Te₃. *Science* **325**, 178 (2009).
 - ⁶ Fu, L. Topological Crystalline Insulators. *Phys. Rev. Lett.* **106**, 106802 (2011).
 - ⁷ Jadaun, P., Xiao, D., Niu, Q. & Banerjee, S. K. Topological classification of crystalline insulators with space group symmetry. *Phys. Rev. B* **88**, 085110 (2013).
 - ⁸ Shiozaki, K. & Sato, M. Topology of crystalline insulators and superconductors. *Phys. Rev. B* **90**, 165114 (2014).
 - ⁹ Wang, Z., Alexandradinata, A., Cava, R. J. & Bernevig, B. A. Hourglass Fermions. *Nature* **532**, 189–194 (2016).
 - ¹⁰ Ma, J. *et al.* Experimental evidence of hourglass fermion in the candidate nonsymmorphic topological insulator KHgSb. *Sci. Adv.* **3**, e1602415 (2017).
 - ¹¹ Fu, L. & Kane, C. L. Topological insulators with inversion symmetry. *Phys. Rev. B* **76**, 045302 (2007).
 - ¹² Wang, Z., Wieder, B. J., Li, J., Yan, B. & Bernevig, B. A. Higher-Order Topology, Monopole Nodal Lines, and the Origin of Large Fermi Arcs in Transition Metal Dichalcogenides XTe₂ (X = Mo, W). *Phys. Rev. Lett.* **123**, 186401 (2019).
 - ¹³ Bradlyn, B. *et al.* Band connectivity for topological quantum chemistry: Band structures as a graph theory problem. *Phys. Rev. B* **97**, 035138 (2018).
 - ¹⁴ Bradlyn, B., Wang, Z., Cano, J. & Bernevig, B. A. Disconnected elementary band representations, fragile topology, and Wilson loops as topological indices: An example on the triangular lattice. *Phys. Rev. B* **99**, 045140 (2019).
 - ¹⁵ Po, H. C., Vishwanath, A. & Watanabe, H. Symmetry-based Indicators of Band Topology in the 230 Space Groups. *Nat. Commun.* **8**, 50 (2017).
 - ¹⁶ Song, Z., Zhang, T., Fang, Z. & Fang, C. Quantitative mappings between symmetry and topology in solids. *Nat. Commun.* **9**, 3530 (2018).
 - ¹⁷ Bradlyn, B. *et al.* Topological quantum chemistry. *Nature* **547**, 298–305 (2017).
 - ¹⁸ Zhang, T. *et al.* Catalogue of topological electronic materials. *Nature* **566**, 475 (2019).
 - ¹⁹ Tang, F., Po, H. C., Vishwanath, A. & Wan, X. Comprehensive search for topological materials using symmetry indicators. *Nature* **566**, 486 (2019).
 - ²⁰ Vergniory, M. G. *et al.* A complete catalogue of high-quality topological materials. *Nature* **566**, 480–485 (2019).
 - ²¹ Hasan, M. Z. & Kane, C. L. Colloquium : Topological Insulators. *Rev. Mod. Phys.* **82**, 3045–3067 (2010).
 - ²² Qi, X.-L. & Zhang, S.-C. Topological insulators and superconductors. *Rev. Mod. Phys.* **83**, 1057–1110 (2011).
 - ²³ Fu, L. & Kane, C. L. Superconducting Proximity Effect and Majorana Fermions at the Surface of a Topological Insulator. *Phys. Rev. Lett.* **100**, 096407 (2008).
 - ²⁴ Yu, R. *et al.* Quantized Anomalous Hall Effect in Magnetic Topological Insulators. *Science* **329**, 61 (2010).
 - ²⁵ Chang, C.-Z. *et al.* Quantized Anomalous Hall Effect in Magnetic Topological Insulators. *Science* **340**, 167 (2013).
 - ²⁶ Li, J. *et al.* Intrinsic magnetic topological insulators in van der Waals layered MnBi₂Te₄-family materials. *Sci. Adv.* **5**, eaaw5685 (2019).
 - ²⁷ Ge, J. *et al.* High-Chern-Number and High-Temperature Quantum Hall Effect without Landau Levels. *Natl. Sci. Rev.* **7**, 1280 (2020).
 - ²⁸ Hor, Y. S. *et al.* Superconductivity in Cu_xBi₂Se₃ and its Implications for Pairing in the Undoped Topological Insulator. *Phys. Rev. Lett.* **104**, 057001 (2010).
 - ²⁹ Wray, L. A. *et al.* Observation of topological order in a superconducting doped topological insulator. *Nat. Phys.* **6**, 855–859 (2010).
 - ³⁰ Xu, J.-P. *et al.* Experimental Detection of a Majorana Mode in the core of a Magnetic Vortex inside a Topological Insulator-Superconductor Bi₂Te₃/NbSe₂ Heterostructure. *Phys. Rev. Lett.* **114**, 017001 (2015).
 - ³¹ Wu, X., Qin, S., Liang, Y., Fan, H. & Hu, J. Topological characters in Fe(Te_{1-x}Se_x) thin films. *Phys. Rev. B* **93**, 115129 (2016).
 - ³² Nie, S. *et al.* Topological phases in the TaSe₃ compound. *Phys. Rev. B* **98**, 125143 (2018).
 - ³³ Oganov, A. R. & Glass, C. W. Crystal structure prediction using ab initio evolutionary techniques: Principles and applications. *J. Chem. Phys.* **124**, 244704 (2006).
 - ³⁴ Oganov, A. R., Lyakhov, A. O. & Valle, M. How Evolutionary Crystal Structure Prediction Works-and Why. *Acc. Chem. Res.* **44**, 227–237 (2011).
 - ³⁵ Lyakhov, A. O., Oganov, A. R., Stokes, H. T. & Zhu, Q. New Developments in Evolutionary Structure Prediction Algorithm USPEX. *Comput. Phys. Commun.* **184**, 1172 (2013).
 - ³⁶ Xia, K. *et al.* A novel superhard tungsten nitride predicted by machine-learning accelerated crystal structure search. *Sci. Bull.* **63**, 817 (2018).
 - ³⁷ Zhang, X., Yu, L., Zakutayev, A. & Zunger, A. Sorting Stable versus Unstable Hypothetical Compounds: The Case of Multi-Functional ABX Half-Heusler Filled Tetrahedral Structures. *Adv. Funct. Mater.* **22**, 1425 (2012).
 - ³⁸ Peng, B., Yue, C., Zhang, H., Fang, Z. & Weng, H. Predicting Dirac semimetals based on sodium ternary compounds. *npj Comput. Mater.* **4**, 68 (2018).
 - ³⁹ Levy, N. *et al.* Strain-Induced Pseudo-Magnetic Fields Greater Than 300 Tesla in Graphene Nanobubbles. *Science* **329**, 544–547 (2010).
 - ⁴⁰ Shao, D. *et al.* Strain-induced quantum topological phase transitions in Na₃Bi. *Phys. Rev. B* **96**, 075112 (2017).
 - ⁴¹ Gao, J., Wu, Q., Persson, C. & Wang, Z. Irvsp: To obtain irreducible representations of electronic states in the VASP. *Comput. Phys. Commun.* **261**, 107760 (2021).
 - ⁴² Perdew, J. P., Burke, K. & Ernzerhof, M. Generalized Gradient Approximation Made Simple. *Phys. Rev. Lett.* **77**, 3865–3868 (1996).
 - ⁴³ Heyd, J., Scuseria, G. E. & Ernzerhof, M. Erratum: "hybrid functionals based on a screened coulomb potential"

- [j. chem. phys. 118, 8207 (2003)]. *J. Chem. Phys.* **124**, 219906 (2006).
- ⁴⁴ Sancho, M. P. L., Sancho, J. M. L. & Rubio, J. Quick iterative scheme for the calculation of transfer matrices: application to Mo (100). *J. Phys. F:Met. Phys.* **14**, 1205 (1984).
- ⁴⁵ Sancho, M. P. L., Sancho, J. M. L., Sancho, J. M. L. & Rubio, J. Highly convergent schemes for the calculation of bulk and surface Green functions. *J. Phys. F:Met. Phys.* **15**, 851 (1985).
- ⁴⁶ Wu, Q., Zhang, S., Song, H.-F., Troyer, M. & Soluyanov, A. A. Wanniertools: An open-source software package for novel topological materials. *Comput. Phys. Commun.* **224**, 405 (2018).
- ⁴⁷ Winkler, R. Spin-Orbit Coupling Effects in Two-Dimensional Electron and Hole Systems. (*Springer Tracts in Modern Physics, Vol. 191, Springer, 2003*) (2003).
- ⁴⁸ Fu, L. & Berg, E. Odd-Parity Topological Superconductors: Theory and Application to $\text{Cu}_x\text{Bi}_2\text{Se}_3$. *Phys. Rev. Lett.* **105**, 097001 (2010).
- ⁴⁹ Fu, L. Odd-Parity Topological Superconductors: Theory and Application to $\text{Cu}_x\text{Bi}_2\text{Se}_3$. *Phys. Rev. B* **90**, 100509 (2014).
- ⁵⁰ Sasaki, S. *et al.* Topological Superconductivity in $\text{Cu}_x\text{Bi}_2\text{Se}_3$. *Phys. Rev. Lett.* **107**, 217001 (2011).
- ⁵¹ Kirzhner, T., Lahoud, E., Chaska, K. B., Salman, Z. & Kanigel, A. Point-contact spectroscopy of $\text{Cu}_{0.2}\text{Bi}_2\text{Se}_3$ single crystals. *Phys. Rev. B* **86**, 064517 (2012).
- ⁵² Bay, T. V. *et al.* Superconductivity in the Doped Topological Insulator $\text{Cu}_x\text{Bi}_2\text{Se}_3$ under High Pressure. *Phys. Rev. Lett.* **108**, 057001 (2012).
- ⁵³ Levy, N. *et al.* Experimental Evidence for s-Wave Pairing Symmetry in Superconducting $\text{Cu}_x\text{Bi}_2\text{Se}_3$ Single Crystals Using a Scanning Tunneling Microscope. *Phys. Rev. Lett.* **110**, 117001 (2013).
- ⁵⁴ Matano, K., Kriener, M., Segawa, K., Ando, Y. & Zheng, G.-q. Spin-rotation symmetry breaking in the superconducting state of $\text{Cu}_x\text{Bi}_2\text{Se}_3$. *Nat. Phys.* **12**, 852 (2016).
- ⁵⁵ Allen, P. B. & Dynes, R. C. Transition temperature of strong-coupled superconductors reanalyzed. *Phys. Rev. B* **12**, 905–922 (1975).
- ⁵⁶ Kresse, G. & Joubert, D. From ultrasoft pseudopotentials to the projector augmented-wave method. *Phys. Rev. B* **59**, 1758–1775 (1999).
- ⁵⁷ Monkhorst, H. J. & Pack, J. D. Special points for Brillouin-zone integrations. *Phys. Rev. B* **13**, 5188–5192 (1976).
- ⁵⁸ Togo, A. & Tanaka, I. First principles phonon calculations in materials science. *Scr. Mater.* **108**, 1 (2015).
- ⁵⁹ Giannozzi, P. *et al.* QUANTUM ESPRESSO: a modular and open-source software project for quantum simulations of materials. *J. Phys. Condens. Matter* **21**, 395502 (2009).
- ⁶⁰ Dong, X. & Fan, C. Rich stoichiometries of stable Ca-Bi system: Structure prediction and superconductivity. *Sci. Rep.* **5**, 9326 (2015).
- ⁶¹ Cheng, X., Li, R., Li, D., Li, Y. & Chen, X.-Q. Stable compositions and structures in the Na-Bi system. *Phys. Chem. Chem. Phys.* **17**, 6933–6947 (2015).
- ⁶² Le, C. *et al.* Three-dimensional topological critical Dirac semimetal in AMgBi ($A = \text{K}, \text{Rb}, \text{Cs}$). *Phys. Rev. B* **96**, 115121 (2017).
- ⁶³ Jain, A., Ong, S. P., Hautier, G. & Wei, C. Commentary: The Materials Project: A materials genome approach to accelerating materials innovation. *APL Mater.* **1**, 011002 (2013).
- ⁶⁴ Hellenbrandt, M. The Inorganic Crystal Structure Database (ICSD) Present and Future. *Crystallogr. Rev.* **10**, 17–22 (2004).
- ⁶⁵ Wang, Z. *et al.* Dirac semimetal and topological phase transitions in A_3Bi ($A = \text{Na}, \text{K}, \text{Rb}$). *Phys. Rev. B* **85**, 195320 (2012).